J. Fluid Mech. (2000), *vol.* 424, *pp.* 21–44. Printed in the United Kingdom

Finite Reynolds number effects in the propagation of an air finger into a liquid-filled flexible-walled channel

By MATTHIAS HEIL

Department of Mathematics, University of Manchester, Oxford Road, Manchester M13 9PL, UK

(Received 14 April 2000 and in revised form 30 June 2000)

This paper investigates finite Reynolds number effects in the problem of the propagation of an air finger into a liquid-filled flexible-walled two-dimensional channel. The study is motivated by the physiological problem of pulmonary airway reopening. A fully consistent model of the fluid–structure interaction is formulated and solved numerically using coupled finite element discretizations of the free-surface Navier–Stokes equations and the Lagrangian wall equations. It is shown that for parameter values which are representative of the conditions in the lung and in typical laboratory experiments, fluid inertia plays a surprisingly important role: even for relatively modest ratios of Reynolds and capillary numbers ($Re/Ca \approx 5$–10), the pressure required to drive the air finger at a given speed increases significantly compared to the zero Reynolds number case. Fluid inertia leads to significant changes in the velocity and pressure fields near the bubble tip and is responsible for a noticeable change in the wall deformation pattern ahead of the bubble. For some parameter variations (such as variations in the wall tension), finite Reynolds number effects are shown to lead to qualitative changes in the system's behaviour. Finally, the implications of the result for pulmonary airway reopening are discussed.

1. Introduction

Many pulmonary diseases result in the collapse and occlusion of parts of the lung with viscous fluid (Pride & Macklem 1986; Macklem, Proctor & Hogg 1970; Hughes, Rosenzweig & Kivitz 1970). The subsequent airway reopening is assumed to occur via the propagation of an 'air finger' into the collapsed, fluid-filled part of the airway (Grotberg 1994). The problem has some similarity to the scenario of the 'first breath' when air has to enter the fluid-filled airways of a newborn baby for the first time. Due to the complex nature of the three-dimensional fluid–structure interaction which governs this problem (a free-surface flow interacting with a strongly collapsed elastic tube), the mechanics of airway reopening are still poorly understood.

The first experimental study of airway reopening was carried out by Gaver, Samsel & Solway (1990) who investigated the propagation of an air finger into a strongly collapsed, thin-walled polyethylene tube which had been filled with oil. The study determined the propagation speed, U, of the air finger as a function of the applied bubble pressure, p_b^*, and derived estimates of physiological airway reopening times via scaling arguments. The authors made the interesting observation that, as the propagation speed U approached zero, $p_b^*(U)$ appeared to approach a finite value. This was interpreted as a yield pressure, i.e. the minimum pressure required to initiate

the motion of the air finger. The airways of the lung are surrounded by a supporting network of parenchyma which act as an elastic bedding for the airway walls. The effect of this 'parenchymal tethering' on the airway reopening characteristics was studied by Yap *et al.* (1994) and Perun & Gaver (1995).

In the experimental investigations, the extremely thin-walled tubes (of wall-thickness-to-radius ratios h_0/R_0 between $1/100$ and $1/1000$) were flattened with a metal plate before the tube was reopened. In this strongly collapsed configuration, the fluid-filled part of the tube has a cross-section of large aspect ratio. This was exploited in Gaver *et al.*'s (1996) theoretical and computational study of airway reopening: the collapsed airway was modelled as an infinitely long two-dimensional channel with elastic walls under axial tension, supported on an elastic bedding. Reopening of the channel was assumed to occur by a propagating semi-infinite bubble. Motivated by the low Reynolds numbers in the experiments, Gaver *et al.* (1996) restricted themselves to zero Reynolds number flows and solved the Stokes equations numerically by a boundary element method. The channel walls were modelled as spring-backed 'strings under tension' and the wall equations were formulated in an Eulerian framework which allowed them to be directly incorporated into the fluid problem. This was possible because the Eulerian wall model (without bending stiffness) yields a traction boundary condition for the fluid whose structure is very similar to the dynamic free-surface condition in the presence of surface tension. Since the Eulerian representation of the wall mechanics does not trace the paths of material particles on the channel walls, the velocity boundary conditions for the fluid had to be based on the *ad hoc* assumption that the wall particles move normal to the wall's centreline as the finger propagates along the channel. Gaver *et al.* (1996) assumed the initial wall tension to be so large that any flow-induced changes to the wall tension could be neglected.

Gaver *et al.* (1996) also developed a lubrication theory approximation for the problem which was shown to be accurate at low capillary number Ca but failed to capture some important features at larger Ca. Recently, Jensen, Horsburgh & Gaver (2000) developed an improved asymptotic model (based on the assumption of large wall tension and small spring stiffness). This improved model successfully captures (at least qualitatively) the behaviour at large capillary numbers.

While elucidating many aspects of the fluid–structure interaction governing the mechanics of airway reopening, Gaver *et al.*'s (1996) boundary element calculations are inherently restricted to zero Reynolds number flows. Such flows might be expected to provide an accurate representation of the fluid mechanics in those experiments in which high-viscosity fluids were used. However, the Reynolds numbers during physiological airway reopening can be quite large and the effect of fluid inertia on the system's behaviour is not clear. Furthermore, any two-dimensional model of airway reopening is incapable of capturing some of the essential features of the three-dimensional system in which an air finger reopens a non-axisymmetrically collapsed cylindrical tube (see § 4 for further discussion of this point). Gaver *et al.*'s (1996) wall model cannot easily be generalized to three dimensions since the inclusion of bending stiffness (which is necessary to capture the tube's post-buckling behaviour) produces wall equations whose structure is significantly different from the 'standard' boundary conditions of fluid mechanics: Hence, in three dimensions, the wall equations cannot be directly incorporated into the fluid equations.

This paper aims to address both of these problems. The two-dimensional airway reopening problem is reformulated in terms of a coupled Eulerian Lagrangian fluid–structure interaction model. The resulting model is fully self-consistent, contains no *ad hoc* boundary conditions and can easily be extended to three dimensions. The

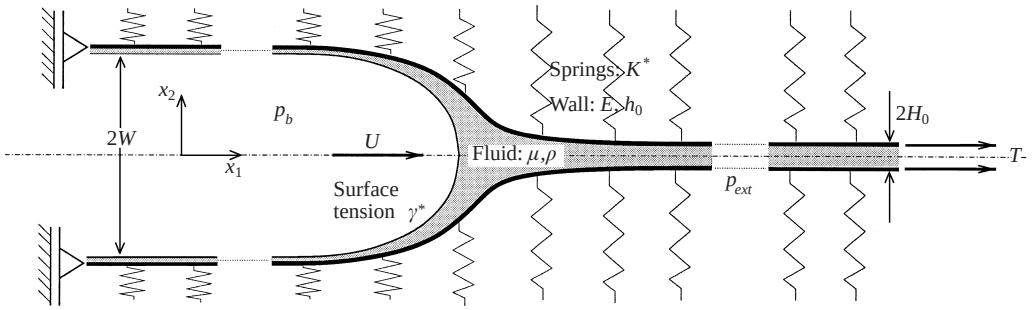

FIGURE 1. Sketch of the model problem: an air finger propagates into a liquid-filled two-dimensional channel with elastic walls.

fluid flow is described by the free-surface Navier–Stokes equations which allows finite Reynolds number effects to be studied. The outline of the paper is as follows. In § 2, the model problem and the governing equations are introduced and the finite element based solution of the fully coupled equations is developed. Section 3.1 reconsiders the system's behaviour at zero Reynolds number: the results obtained from the Lagrangian wall model are compared to those from Gaver *et al.*'s (1996) Eulerian wall model and the origin of the discrepancies between the two models is discussed. Section 3.2 investigates the effect of finite Reynolds numbers and identifies the two main mechanisms by which fluid inertia affects the system's behaviour. Section 3.3 shows that fluid inertia can lead to qualitative changes of the system's behaviour in response to changes in the wall parameters such as the wall tension. Finally, § 4 assesses the relevance of the results in the context of the pulmonary airway reopening problem.

2. The model

Figure 1 shows a sketch of the model problem to be investigated in this study. Inside a flexible-walled two-dimensional channel, a positive bubble pressure p_b^* drives an air finger into a fluid of viscosity μ, density ρ and surface tension γ^*. The finger propagates at a steady speed U and separates the spring-backed elastic walls which are subject to an axial tension T. Far ahead of and far behind the bubble tip, the walls are separated by a distance $2H_0$ and $2W$, respectively. Without loss of generality, we assume that (i) far ahead of the bubble tip, the linear springs are in their stress-free position and (ii) the external pressure is $p_{ext} = 0$. This implies that the fluid pressure far ahead of the bubble tip must also tend to zero. Note that assumptions (i) and (ii) are possible because we assume the channel width $2H_0$ to be given. Any change to the springs' rest position could be compensated for by a corresponding change to the external pressure and vice versa. Any uncompensated change to p_{ext} would manifest itself in a change to the channel width H_0. This is a particular feature of the two-dimensional problem which is absent in three dimensions. As in Gaver *et al.*'s (1996) study, we assume that the system remains symmetric about the channel's centreline and only model the lower half of the domain.

2.1. *The wall equations*

We model the elastic channel walls as pre-stressed elastic beams of thickness h_0, supported on an elastic foundation of stiffness K^*. We describe the beam's deformation in terms of its dimensionless centreline displacement $\boldsymbol{v} = \boldsymbol{v}^*/H_0$ which is a function of the non-dimensional Lagrangian coordinate $\xi = \xi^*/H_0$, measured along the beam's centreline. Throughout this paper, a superscript star distinguishes dimensional

quantities from their non-dimensional equivalents. Time is non-dimensionalized as $t = t^* U/H_0$ and all lengths are scaled by H_0. In a frame moving with the velocity U of the bubble tip, the non-dimensional position vector to a material point on the channel wall is then given by $\boldsymbol{R}_w(\xi, t) = \boldsymbol{R}_w(\zeta) = (\zeta + v^1(\zeta), -1 + v^2(\zeta))$ where v^1 and v^2 are the displacement components of material points in the x_1- and x_2-directions, respectively. $\zeta = \xi - t$ is the non-dimensional Lagrangian travelling wave coordinate. In the travelling wave frame, the velocity of material points on the wall is given by $\partial \boldsymbol{R}_w/\partial t = -(1 + v^1_{,\zeta}, v^2_{,\zeta})$, where subscript commas indicate partial differentiation.

The elastic walls are subject to a large initial tension $\sigma_0^* = T/h_0$ which is generated by the force T acting at the far right-hand end of the system. We assume the additional strain due to the wall's deformation to be small enough to justify the use of an incrementally linear constitutive equation, such that $\sigma = \sigma_0 + \epsilon$ where $\sigma = \sigma^*/E$ is the dimensionless second Piola–Kirchhoff stress, $\sigma_0 = \sigma_0^*/E$ is the dimensionless pre-stress, E is the incremental Young's modulus and ϵ is the geometrically nonlinear strain $\epsilon = v^1_{,\zeta} + \frac{1}{2}((v^1_{,\zeta})^2 + (v^2_{,\zeta})^2)$. For thin channel walls, we do not expect wall inertia to play a significant role in the problem. With these assumptions, the principle of virtual displacements which governs the wall deformation is given by

$$\int_{-\infty}^{\infty} \left[(\sigma_0 + \epsilon)\delta\epsilon + \frac{1}{12}\left(\frac{h_0}{H_0}\right)^2 \kappa\, \delta\kappa \right.$$
$$\left. - \left(\frac{H_0}{h_0}\right)(\boldsymbol{f} \cdot \delta \boldsymbol{R}_w \sqrt{(1 + v^1_{,\zeta})^2 + (v^2_{,\zeta})^2} - K v^2 (1 + v^1_{,\zeta})\delta v^2) \right] \mathrm{d}\zeta = 0, \qquad (2.1)$$

where $\boldsymbol{f} = \boldsymbol{f}^*/E$ is the non-dimensional traction acting on the wall and $K = K^* H_0/E$ is the non-dimensional stiffness of the uniformly distributed springs which are assumed to remain vertical at all times. $\kappa = (v^2_{,\zeta\zeta}(1 + v^1_{,\zeta}) - v^1_{,\zeta\zeta} v^2_{,\zeta}) \Big/ \sqrt{(1 + v^1_{,\zeta})^2 + (v^2_{,\zeta})^2}$ represents the non-dimensional change of curvature of the wall's centreline. The physical interpretation of the various terms in (2.1) is as follows: the first two terms represent the variation in the wall's strain energy due to its extension and bending, respectively; the last two terms represent the virtual work done by the fluid traction $\boldsymbol{f}$ (acting on the deformed wall) and by the uniformly distributed springs, respectively. A more detailed discussion of the large-displacement beam theory can be found in Wempner (1973).

Carrying out the variations with respect to the displacements v^i and their derivatives transforms equation (2.1) into a variational equation of the form

$$\int_{-\infty}^{\infty} (\phi_i^{(0)}\ \delta v^i + \phi_i^{(1)}\ \delta v^i_{,\zeta} + \phi_i^{(2)}\ \delta v^i_{,\zeta\zeta})\, \mathrm{d}\zeta = 0, \qquad (2.2)$$

where the ϕ-terms contain up to second derivatives of the displacements and the summation convention is used.

In a finite region surrounding the bubble tip ($\zeta_L < \zeta < \zeta_R$), we discretize this variational equation by displacement-based finite elements. Since the integrand contains up to second derivatives of the displacements, we need shape functions with continuous first derivatives across the element boundaries. Isoparametric Hermite elements with nodal displacements and slopes as independent degrees of freedom (Bogner, Fox & Schmit 1967) were chosen such that the displacements v^i were interpolated as

$$v^i = \sum_{j,k} V^{ijk} \psi_{jk}, \qquad (2.3)$$

where the ψ_{jk} are piecewise Hermite polynomials. In terms of the local node numbers and the local element coordinate, $s \in [0,1]$, these shape functions are given by $\psi_{11}(s) = 2s^3 - 3s^2 + 1$, $\psi_{12}(s) = s^3 - 2s^2 + s$, $\psi_{21}(s) = -(2s^3 - 3s^2)$ and $\psi_{22}(s) = s^3 - s^2$. The first index of the shape function ψ_{jk} stands for the local node number ($j = 1, 2$); the shape function's second index ($k = 1, 2$) stands for the type of degree of freedom, interpolating the displacement or the derivative with respect to the local coordinate s, respectively.

To generate isoparametric elements, the same shape functions were used to map the local coordinate s to the global Lagrangian coordinate ζ,

$$\zeta = \sum_{j,k} Z^{jk} \psi_{jk}. \tag{2.4}$$

Details of the choice of the coefficients Z^{jk} can be found in Heil & Pedley (1996).

We insert (2.3) and (2.4) into (2.2) and obtain

$$\left\{ \int_{\zeta_L}^{\zeta_R} (\phi_i^{(0)} \psi_{jk} + \phi_i^{(1)} \psi_{jk,\zeta} + \phi_i^{(2)} \psi_{jk,\zeta\zeta}) \, \mathrm{d}\zeta \right\} \delta V^{ijk} + \Phi_{ijk} \delta V^{ijk} = 0, \tag{2.5}$$

where the last term contains the boundary contributions which arise from the truncation of the domain (see the Appendix). The variations of those V^{ijk} which are not determined by the boundary conditions are arbitrary and the expressions multiplied by the corresponding δV^{ijk} have to vanish. This provides a system of nonlinear algebraic equations for the unknown V^{ijk}. These equations still contain the load terms $\boldsymbol{f}$, which have to be determined from the solution of the fluid equations. The integrals over the elements were evaluated using a three-point Gauss rule.

2.2. *The fluid equations*

In a frame moving steadily with the velocity U of the bubble tip, the flow is described by the non-dimensional Navier–Stokes equations

$$Re \, u_j \frac{\partial u_i}{\partial x_j} = -\frac{\partial p}{\partial x_i} + \frac{\partial}{\partial x_j} \left(\frac{\partial u_i}{\partial x_j} + \frac{\partial u_j}{\partial x_i} \right) \tag{2.6}$$

and the continuity equation

$$\frac{\partial u_i}{\partial x_i} = 0, \tag{2.7}$$

where we have scaled the velocities with the bubble velocity, i.e. $u_i = u_i^*/U$, and have used the viscous pressure scale, i.e. $p = p^*/(\mu U/H_0)$. The Reynolds number is defined as $Re = UH_0\rho/\mu$. On the free fluid surface, whose outer unit normal we denote by $\boldsymbol{n}$, the fluid normal velocity vanishes,

$$\boldsymbol{u} \cdot \boldsymbol{n} = 0 \quad \text{on the air–liquid interface,} \tag{2.8}$$

and the dynamic boundary condition implies that

$$-pn_i + \left(\frac{\partial u_i}{\partial x_j} + \frac{\partial u_j}{\partial x_i} \right) n_j + \frac{1}{Ca} \kappa_f n_i = -p_b n_i \quad \text{on the air–liquid interface.} \tag{2.9}$$

$\kappa_f = \kappa_f^* H_0$ is the non-dimensional interface curvature and $Ca = U\mu/\gamma^*$ is the capillary number which can be regarded as the non-dimensional bubble velocity.

The numerical technique employed to solve the fluid equations on the variable domain which is enclosed by the free air–liquid interface and the deforming wall is

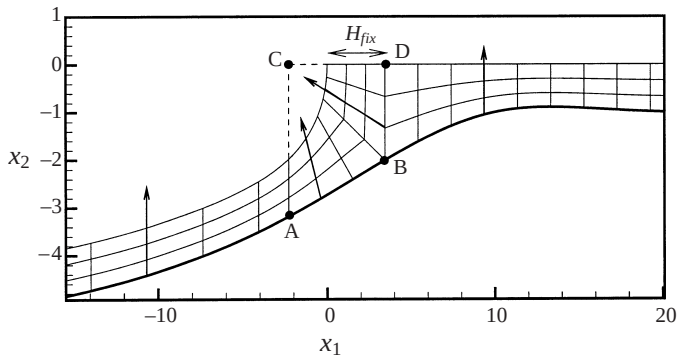

FIGURE 2. Sketch illustrating the automatic fluid mesh generation. The arrows illustrate the direction of representative spines in the different regions of the fluid domain.

illustrated in figure 2. In the region $\zeta_l < \zeta < \zeta_r$, the fluid domain is decomposed into finite elements whose nodal positions are determined by the method of spines (Kistler & Scriven 1983). For this purpose we parameterize the free-surface position by its 'height' $h(\zeta)$ 'above' the channel wall. The 'height' is measured in the direction of certain pre-determined unit vectors $\boldsymbol{S}$ (the spines) which emanate from the wall and from a vertical line (B to D) across the channel. The direction of the spines is varied as a function of the Lagrangian wall coordinate ζ: away from the bubble tip (i.e. left of point A and right of point B), the spines point vertically upwards; near the bubble tip (i.e. between points A and B) the spines point towards a central point (point C, which is located vertically above point A) on the channel's centreline. As the wall deforms, points A and B remain attached to the same material points on the wall. Since the spines emanate from given material points on the wall, we can use the Lagrangian wall coordinate ζ to parameterize the free surface as

$$\boldsymbol{R}_h(\zeta) = \boldsymbol{R}_w(\zeta) + h(\zeta)\boldsymbol{S}(\zeta). \tag{2.10}$$

The spines not only resolve the free-surface position but also facilitate the automatic adjustment of the fluid mesh to changes in the fluid domain. We associate each nodal point j in the fluid mesh with a fixed material point on the channel wall and identify it by its Lagrangian coordinate $\zeta_j^{(ref)}$. As the wall and the free surface deform, the fluid node remains located at a fixed, predetermined fraction $\omega_j \in [0,1]$ along its spine such that the position vector to fluid node j is given by

$$\boldsymbol{R}_j = \boldsymbol{R}_w(\zeta_j^{(ref)}) + \omega_j\, h(\zeta_j^{(ref)})\, \boldsymbol{S}(\zeta_j^{(ref)}). \tag{2.11}$$

We discretize the fluid equations with standard isoparametric Taylor–Hood-type elements such that the velocities, the global coordinates and the pressure (relative to the bubble pressure p_b) are represented by

$$u_i = \sum_j U^{ij}\psi_j^{(F)}, \quad x_i = \sum_j X^{ij}\psi_j^{(F)} \quad \text{and} \quad p = p_b + \sum_j P^j\psi_j^{(P)}, \tag{2.12}$$

where the $\psi_j^{(F)}$ and $\psi_j^{(P)}$ are bi-quadratic and bi-linear shape functions in the local element coordinates, respectively. The reduced order of the pressure interpolation is required to satisfy the LBB condition (see, e.g., Sani *et al.* 1981). X^{ij} are the nodal coordinates, given by (2.11). The free-surface height $h(\zeta)$ is discretized by

one-dimensional isoparametric quadratic elements such that

$$h = \sum_j H^j \psi_j^{(H)} \quad \text{and} \quad \zeta = \sum_j \tilde{Z}^j \psi_j^{(H)}, \tag{2.13}$$

where $\tilde{Z}^j = \zeta_j^{(ref)}$ and the $\psi_j^{(H)}$ are one-dimensional piecewise quadratic shape functions in the local element coordinate. The heights H^j in the fluid-filled region ahead of the bubble tip are determined by the wall displacement field via $H^j = 1 - v^2(\zeta_j^{(ref)})$, since the fluid domain has to extend up to the channel's centreline. The height $H^{j_{tip}}$ which is associated with the fluid node j_{tip} at the bubble tip is determined by the requirement that this node remains at the origin, i.e.

$$H^{j_{tip}} = h_{fix} = \zeta_{j_{tip}}^{(ref)} + v^1(\zeta_{j_{tip}}^{(ref)}). \tag{2.14}$$

The remaining heights H^j define the free-surface position and have to be determined as part of the solution.

The residuals of the momentum equations (2.6) are weighted by the velocity shape functions $\psi_l^{(F)}$ and the dynamic boundary condition (2.9) is incorporated via partial integration (Ruschak 1980). This yields

$$f_{il}^{(F)} = \iint \left[Re\, u_j \frac{\partial u_i}{\partial x_j} \psi_l^{(F)} - (p - p_b) \frac{\partial \psi_l^{(F)}}{\partial x_i} + \left(\frac{\partial u_i}{\partial x_j} + \frac{\partial u_j}{\partial x_i} \right) \frac{\partial \psi_l^{(F)}}{\partial x_j} \right] \mathrm{d}v + \frac{1}{Ca} \int t_i \frac{\partial \psi_l^{(F)}}{\partial S} \, \mathrm{d}S - \frac{1}{Ca} t_i \psi_l^{(F)} \Big|_{x_1 = \zeta_l + v^1(\zeta_l)}^{x_1 = 0}, \tag{2.15}$$

where $\iint \mathrm{d}v$ is the integral over the computational domain, S is the arclength along the free surface and t_i represents the components of its unit tangent vector. Similarly the continuity equation (2.7) is weighted with the bilinear pressure shape functions $\psi_l^{(P)}$ which yields

$$f_l^{(P)} = \iint \frac{\partial u_j}{\partial x_j} \psi_l^{(P)} \, \mathrm{d}v = 0. \tag{2.16}$$

Finally, weighting the kinematic free-surface condition (2.8) by the one-dimensional quadratic shape functions $\psi_l^{(H)}$ provides the equations which determine the unknown free-surface heights H^j via

$$f_l^{(H)} = \int u_j n_j \psi_l^{(H)} \, \mathrm{d}S = 0. \tag{2.17}$$

2.3. *Fluid–solid coupling*

Gaver *et al.* (1996) reported a non-uniqueness in the $Ca(p_b)$ relationship. Therefore we formulate the fluid–solid coupling such that we can prescribe the capillary number Ca and obtain the corresponding bubble pressure p_b as part of the solution. We use a Newton–Raphson method to solve the fully coupled system of equations. Hence, at every stage of the iteration, the latest iterates for the fluid and solid variables are available.

For a given wall shape, the boundary conditions for the fluid equations are as follows. On the channel walls, the no-slip condition forces the fluid to move with the local wall velocity, i.e.

$$\boldsymbol{u} = -(1 + v^1_{,\zeta}, v^2_{,\zeta}) \quad \text{on the wall.} \tag{2.18}$$

Far ahead of the bubble tip, the wall strain tends to zero (see below) and the wall approaches its stress-free position at $x_2 = -1$. The corresponding plug flow velocity profile generates a volume flux of $q = \int u_1 \, dx_2 = -1 = \text{const}$. We truncate the Navier–Stokes domain far ahead of the bubble tip at $\zeta = \zeta_r$ where ζ_r is chosen such that at this point the wall slope $\hat{\beta}$ is small enough to allow us to describe the flow by lubrication theory (which applies at finite Reynolds number provided $\hat{\beta} Re \ll 1$). Then the inflow velocity profile at $\zeta = \zeta_r$ is given by

$$u_1 = \frac{2 - 3w + w^3 - 3x_2{}^2 w}{2(w-1)^3} \tag{2.19}$$

and

$$u_2 = -\frac{w'}{2} \frac{x_2 \left(2wx_2^2 + 6w - 3w^2 - 3 + x_2^2\right)}{(1-w)^4}, \tag{2.20}$$

where $w = v^2$ and $w' = dv^2/d\zeta$ at $\zeta = \zeta_r$. As $\zeta \to -\infty$ the film thickness approaches a constant value which cannot be determined *a priori* since the wall strain far behind the bubble is not known – this is an important difference to Gaver *et al.*'s (1996) inextensible wall model. We truncate the Navier–Stokes domain behind the bubble tip at $\zeta = \zeta_l$ where the flow has become approximately parallel to the wall. Hence on the outflow boundary, we set $\boldsymbol{u} = \boldsymbol{u}|_{wall}$, which is known from (2.18), and leave the film thickness undetermined. The symmetry boundary condition on the channel's centreline requires that $u_2 = 0$ for $x_2 = 0$ and $x_1 > 0$. The stress balance at the free surface is automatically fulfilled since the dynamic boundary condition has already been incorporated into the weak form of the momentum equation, (2.15). The weak form of the kinematic boundary condition, (2.17), provides the equations which determine the unknown film thickness parameters H^j. Note that it is not possible to directly prescribe the position of the bubble tip by setting $H^{j_{tip}} = h_{fix}$ on the spine emanating from point D in figure 2 as this would not allow us to enforce the kinematic boundary condition, $\boldsymbol{u} \cdot \boldsymbol{n} = 0$, at this point. The equation $H^{j_{tip}} = h_{fix}$ must be treated as the equation which determines the unknown bubble pressure p_b. With these boundary conditions, the fluid problem is fully specified and we can formulate the boundary conditions for the solid domain: given the current values of the fluid variables, we obtain the traction $\boldsymbol{f}$ (in the solid non-dimensionalization) that the fluid exerts on the wall from

$$f_i = Ca\,\gamma \left(p n_i - \left(\frac{\partial u_i}{\partial x_j} + \frac{\partial u_j}{\partial x_i} \right) n_j \right) \quad \text{on the wall,} \tag{2.21}$$

where the non-dimensional surface tension

$$\gamma = \frac{\gamma^*}{E H_0} \tag{2.22}$$

represents the ratio of the fluid surface tension to the wall's extensional stiffness. The n_i are the components of the outer unit normal on the fluid domain. As in Gaver *et al.* (1996), we determine the fluid traction on the wall in the regions outside the Navier–Stokes domains (i.e. for $\zeta > \zeta_r$ and $\zeta < \zeta_l$) from lubrication theory (see the Appendix). To suppress rigid body motions, we set the horizontal wall displacement at the left end of the computational domain to $v^1(\zeta_L) = 0$.

The coupled system of discretized equations was solved by a Newton–Raphson method in conjunction with an adaptive continuation technique to perform parameter variations. The off-diagonal blocks in the Jacobian matrix (which arise from the

interaction between fluid and solid variables) were generated by finite differencing, taking advantage of the sparsity of the matrix. Demmel *et al.*'s (1999) SuperLU solver with minimum degree ordering of the equations was used to solve the sparse but poorly structured linear systems. The wall discretization typically extended from $\zeta_L = -300$ to $\zeta_R = 140$ while the Navier–Stokes domain was located between $\zeta_l = -40$ and $\zeta_r = 80$. The standard discretization for the parameter studies presented below involved approximately 4100 degrees of freedom. Selected computations were repeated with a finer resolution of approximately 6100 degrees of freedom to check the mesh convergence of the results – see figure 6. Further validations included a study of the rigid-walled Bretherton problem at zero and finite Reynolds number (Bretherton 1961; Giavedoni & Saita 1997) and a comparison with Gaver *et al.*'s (1996) zero Reynolds number BEM results – see figure 3(*a*). At the standard resolution, a converged solution was typically obtained within a few minutes of CPU time on a DEC Alpha 433au workstation.

The quadratic convergence rate of the Newton–Raphson method and the ability to adaptively change the parameter increments in regions of rapid change provides a very robust and efficient computational procedure. However, the method requires the provision of a good initial guess for all variables. This initial guess was generated by the following initial sequence of calculations which were performed at zero Reynolds number: (i) subject the elastic wall to a step pressure distribution which deforms it into a shape which vaguely resembles the anticipated channel geometry (as sketched in figure 1); (ii) keeping the wall shape from step (i) fixed, compute the fluid flow in the channel. For this calculation an initial guess for the position of the air–liquid interface is required. This was provided by using an initial fluid domain, in which a region of constant film thickness far behind the bubble tip was smoothly merged to the bubble tip whose shape was approximated by a circular arc; (iii) perform a fully coupled calculation in which the traction on the wall is slowly changed from the prescribed pressure (from step (i)) to the actual fluid traction. At the end of this calculation, we obtain a configuration in which the traction generated by the fluid flow in the deformed channel exactly balances the elastic restoring forces and thus keeps the system in overall equilibrium. This configuration was used as the initial guess for all subsequent parameter variations.

3. Results

Unless stated otherwise all results were obtained using parameter values which correspond to Gaver *et al.*'s (1996) 'basic state' in which the ratio η of wall tension to surface tension is

$$\eta = \frac{T}{\gamma^*} = \frac{\sigma_0 h_0}{\gamma H_0} = 100 \tag{3.1}$$

and the ratio of spring stiffness to surface tension forces is

$$\Gamma = \frac{K^* H_0^2}{\gamma^*} = \frac{K}{\gamma} = 0.5. \tag{3.2}$$

To facilitate comparisons with Gaver *et al.*'s (1996) wall model (which did not include bending stiffness) we use a small wall thickness $h_0/H_0 = 5 \times 10^{-4}$ which ensures that bending effects are relatively unimportant. The effect of variations in the wall thickness will be discussed in § 3.3.3.

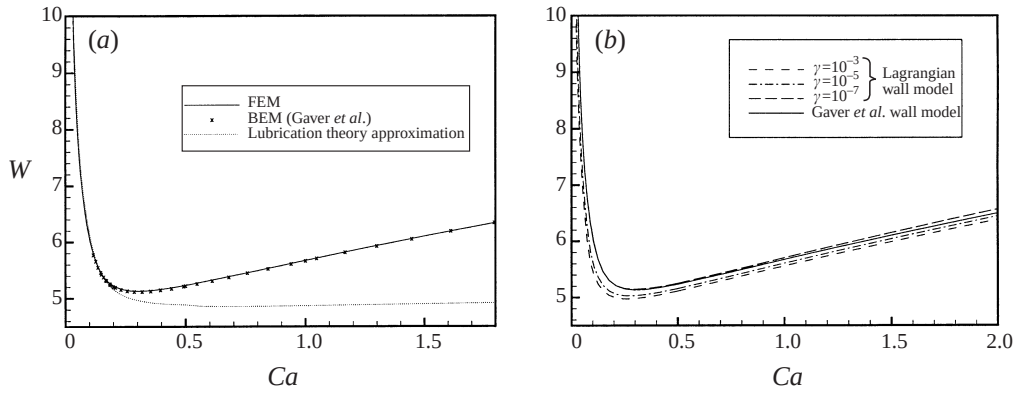

FIGURE 3. Channel width W versus non-dimensional bubble speed $Ca = U\mu/\gamma^*$. (*a*) The FEM predictions compared to Gaver *et al.*'s (1996) BEM computations and the results from their lubrication theory analysis. In all cases, Gaver *et al.*'s (1996) wall equations and velocity boundary conditions were used. (*b*) The predictions from the Lagrangian wall model for various values of the non-dimensional surface tension $\gamma = \gamma^*/(EH_0)$ compared to the predictions from Gaver *et al.*'s (1996) Eulerian wall model. $Re = 0$, $\eta = 100$, $\Gamma = 0.5$.

3.1. *Zero Reynolds number flows*

In order to validate the newly developed code, we first repeated selected computations from Gaver *et al.*'s (1996) study. For this purpose we suppressed the longitudinal displacement by setting $v^1 = 0$ and changed the variational expressions in (2.2) such that the corresponding Euler Lagrange equations represented Gaver *et al.*'s (1996) wall equations. Furthermore, we changed the velocity boundary conditions (2.18) to those used by Gaver *et al.* (1996), namely

$$\boldsymbol{u} = (n_1^2 - 1, n_1 n_2) \quad \text{on the wall.} \tag{3.3}$$

Figure 3(*a*) shows the resulting predictions for the channel width W far behind the bubble tip as a function of the non-dimensional bubble speed $Ca = U\mu/\gamma^*$. The solid line and the symbols represent the predictions from the current FEM code and from Gaver *et al.*'s (1996) BEM computations, respectively. The dotted line represents the results from Gaver *et al.*'s (1996) lubrication theory model which is asymptotically valid in the small-Ca regime. We observe excellent agreement between the three models in their joint regions of validity. Note the two-branch behaviour of the W, Ca characteristics: In the low-Ca regime, all models predict a negative slope for the W, Ca curve. Since, for constant Γ, the channel width W is proportional to the bubble pressure p_b, this implies that in this regime a *decrease* in bubble pressure p_b is required to *increase* the bubble speed U. This is contrary to physical expectation and to the experimental findings. Gaver *et al.* (1996) speculate that this solution branch is unstable. For sufficiently large Ca, the slope of the W, Ca curve becomes positive and represents the physically expected behaviour. Figure 4 shows the shapes of the fluid domains and the corresponding streamlines for four different values of Ca. The contours represent the fluid pressure on the capillary pressure scale which is the relevant scale for the wall deformation; see (2.21). These plots illustrate the different behaviour of the system on the two solution branches. For small Ca, a large volume of fluid is being 'pushed' ahead of the bubble and a closed vortex develops inside the relatively stagnant fluid region just ahead of the bubble tip (see figure 9

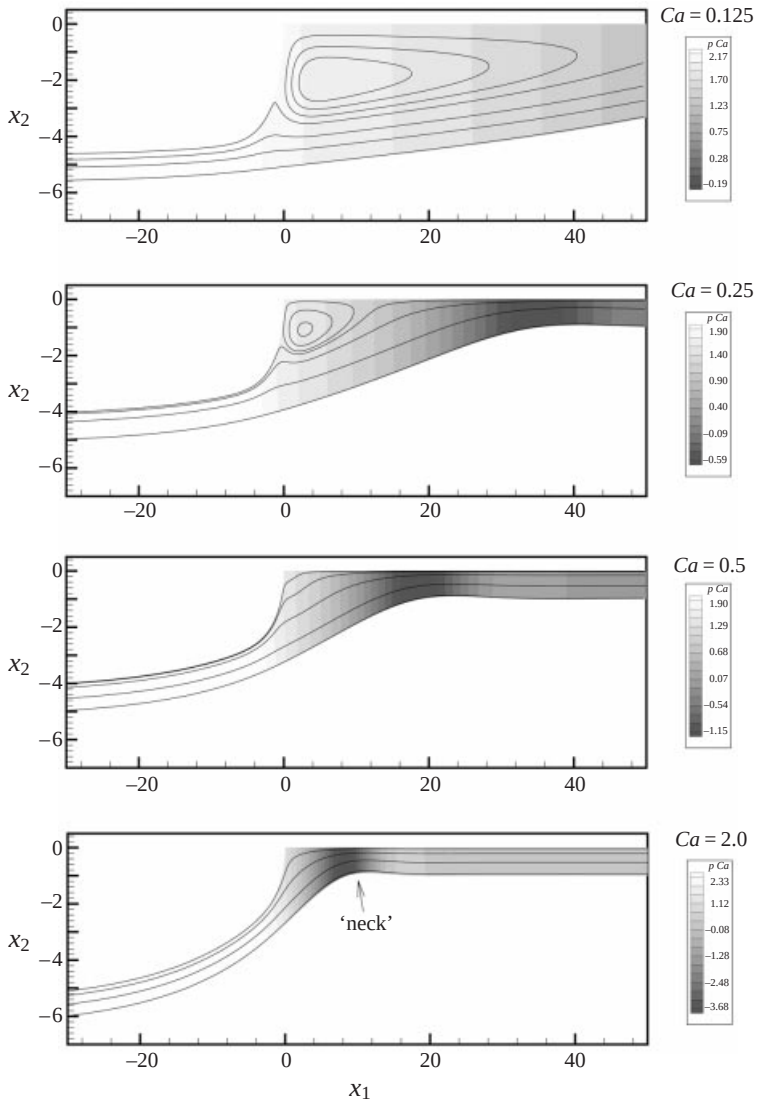

FIGURE 4. Streamlines and contours of the bubble pressure (on the capillary scale), $p_b Ca$, for various Ca. Results are based on Gaver *et al.*'s (1996) wall equations and velocity boundary conditions; $Re = 0$, $\eta = 100$, $\Gamma = 0.5$.

for a representative illustration of the distribution of the absolute velocity). As Ca increases, the length of the transition region over which the channel width adjusts itself to the uniform value far ahead of the bubble tip is reduced: For large Ca, the bubble appears to 'peel' the wall off the fluid layer ahead of the bubble tip. This motivated Gaver *et al.* (1996) to introduce the terms 'pushing' and 'peeling' for the system's behaviour in these two regimes. Notice that figure 4 shows the presence of a 'neck' in the fluid domain near the end of the transition region ahead of the bubble tip. The pressure contours show that at this point, the walls are pulled inwards by a large negative fluid pressure. Gaver *et al.*'s (1996) asymptotic analysis of the system's behaviour far ahead of the bubble tip shows that this 'neck' is generated by the

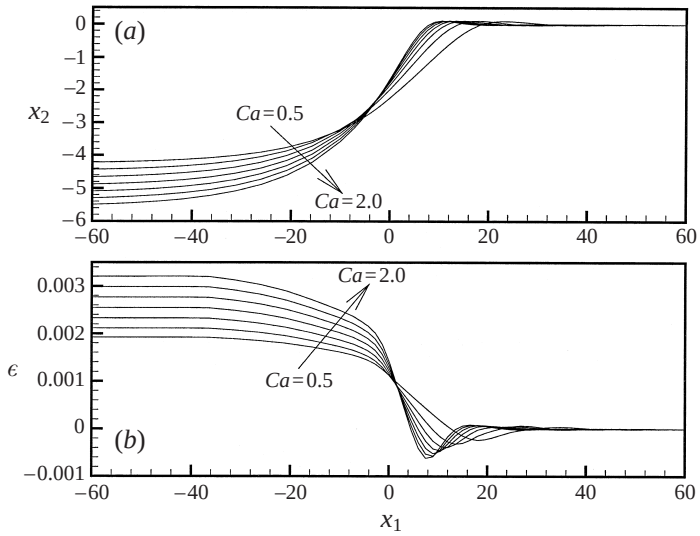

FIGURE 5. The wall shape (a) and the incremental strain distribution ϵ (b) in the vicinity of the bubble tip for the Lagrangian wall model. All Ca values lie on the 'peeling' branch and the increments in Ca between the curves are constant. $\gamma = \gamma^*/(EH_0) = 10^{-7}$, $Re = 0$, $\eta = 100$, $\Gamma = 0.5$.

first (and hence largest) maximum of the damped oscillatory eigensolution for the vertical wall displacement field (see the Appendix). In all cases, the transverse pressure gradient remains small, even in the non-parallel flow region near the bubfle tip.

Figure 3(b) shows a comparison between Gaver *et al.*'s (1996) predictions for the W, Ca relationship and the results obtained from the Lagrangian wall model. Recall that in the Lagrangian wall model, the wall tension is not assumed to be constant but is allowed to vary in response to the traction that the fluid exerts on it. Since the ratio of wall pre-stress to surface tension is kept at a constant large value of $\eta = 100$, the flow-induced variation in the wall tension is relatively small – as it should be if the incrementally linear constitutive equations used in the Lagrangian wall model are to hold. Consequently, there is good qualitative agreement between the models, both of which predict the two-branch behaviour discussed earlier.

In order to elucidate the origin of the discrepancies between the models, figure 5 shows the wall shapes and the corresponding incremental wall strain distribution in the vicinity of the bubble tip. All solutions correspond to Ca values on the 'peeling' branch. The fluid flow far ahead of the bubble tip approaches a plug flow profile and the wall shear stress tends to zero as $x_1 \to \infty$. Consequently, the flow-induced variation of the wall tension tends to zero as well and the wall tension approaches the pre-stress σ_0 which is generated by the force applied at the 'right-hand end' of the wall. Hence the incremental stress and strain both tend to zero as $x_1 \to \infty$. Far behind the bubble tip, the incremental strain is determined by the overall balance of forces which requires that (in dimensional terms)

$$p_b^* W^* = h_0 \epsilon E + \gamma^*. \tag{3.4}$$

On the 'peeling' branch, both bubble pressure p_b^* and airway width W^* increase with Ca, therefore the wall tension far behind the bubble tip has to increase via an increase in the incremental strain ϵ. It is interesting to observe that the incremental wall strain

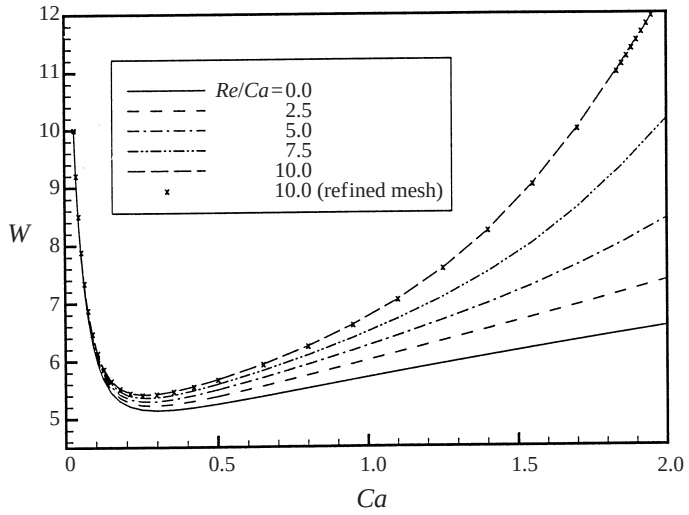

FIGURE 6. Channel width W versus the non-dimensional bubble speed $Ca = U\mu/\gamma^*$ for various values of Re/Ca. The lines represent the data obtained with the standard resolution. The symbols on the $Re/Ca = 10$ curve represent data points obtained with a finer spatial resolution. $\eta = 100$, $\Gamma = 0.5$.

ϵ in the vicinity of the 'neck' region is negative. This indicates that the fluid traction on the wall in this region leads to a slight reduction in the wall tension.

Note that in the Lagrangian wall model, the change in wall tension not only affects the local balance of forces in the wall, but it also affects the velocity boundary conditions for the fluid since, in the travelling wave frame, the fluid velocity varies with the wall strain (see (2.18)). This effect is responsible for the influence of the non-dimensional surface tension γ on the W, Ca curves. Note that $\gamma = \gamma^*/(H_0 E)$ can be expressed in terms of the wall tension parameter η as $\gamma = \sigma_0^* h_0/(H_0 \eta E)$. This shows that for parameter variations in which the ratio of wall pre-stress and surface tension, η, is kept constant, large values of γ correspond to small values of the incremental elastic modulus E. Smaller values of E require larger incremental strains, ϵ, to generate the wall tension increment required by the overall force balance (3.4). Therefore, large values of γ induce large strain-induced variations of the fluid velocity on the wall. Since the latter effect is absent in Gaver *et al.*'s inextensible wall model, the discrepancy between the two models increases with γ. This can clearly be seen in figure 3(b) which also shows that an increase in γ leads to a slight reduction in the bubble pressure required to drive the bubble at a given speed.

When comparing the two wall models, it should be noted that even for large η (corresponding to small flow-induced variations in the wall tension) and $\gamma \to 0$ (corresponding to an increasingly inextensible wall), we do not obtain perfect agreement because of the different velocity boundary conditions, (2.18) and (3.3), respectively, used in the two models.

Finally, note that self-consistency of the Lagrangian wall model requires $\epsilon \ll 1$ to justify the use of the incrementally linear constitutive equation. An examination of the maximum incremental wall strains for the parameter range illustrated in figure 3(b) confirms that ϵ scales inversely with γ. For $\gamma = 10^{-7}$ we have $\epsilon_{max} = O(10^{-3})$ within the parameter range considered in that figure. We use this value for all subsequent parameter studies.

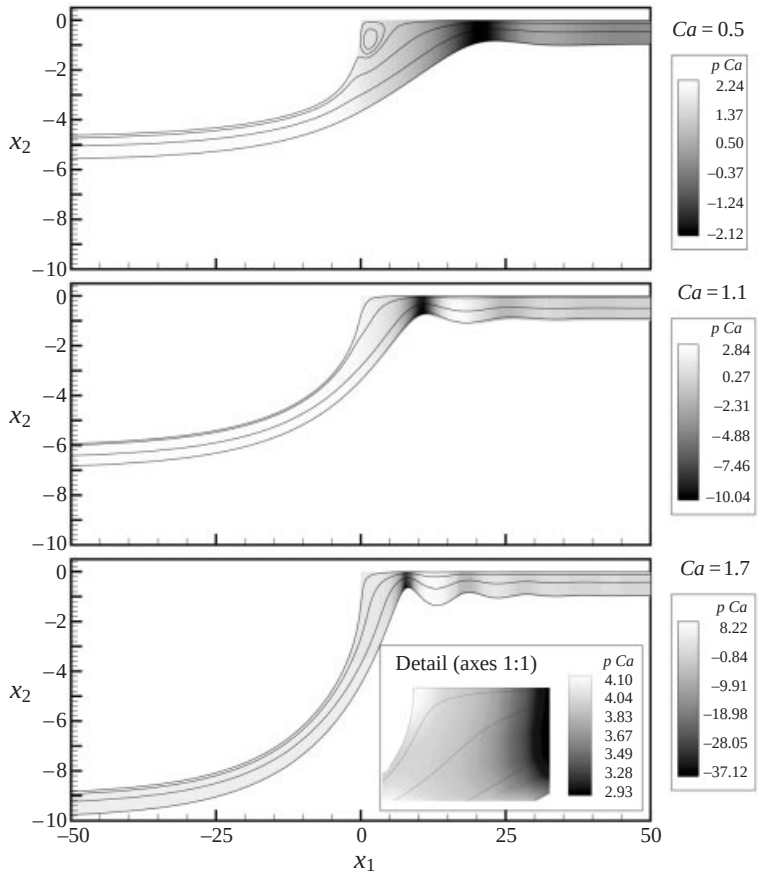

FIGURE 7. Streamlines and pressure contours (on the capillary pressure scale) for various Ca and for $Re/Ca = 10$. $\eta = 100$, $\Gamma = 0.5$.

3.2. *Finite Reynolds number flows*

We will now investigate the effects of fluid inertia on the system's behaviour. Note that in an experiment in which the bubble speed U is controlled by varying the bubble pressure p_b, the ratio of the two fluid dynamical parameters, $Ca = U\mu/\gamma^*$ and $Re = U\rho H/\mu$, remains constant and is given by

$$\frac{Re}{Ca} = \frac{\rho H \gamma^*}{\mu^2} \tag{3.5}$$

since both quantities scale linearly with U. Figure 6 shows the channel width, W, far behind the bubble tip versus the non-dimensional bubble speed $Ca = U\mu/\gamma^*$ for zero and finite fluid inertia. The ratio Re/Ca is kept constant along the different curves, hence on all curves inertial effects become negligible on the 'pushing' branch where Ca and $Re \to 0$. On the 'peeling' branch, an increase in Ca is accompanied by a proportional increase in Re. Figure 6 shows that even for moderate values of Re/Ca, the pressure p_b required to drive the air finger at a given speed increases significantly compared to the zero Reynolds number case. Figure 7 shows the corresponding flow fields and the fluid pressure distributions for different values of Ca and for $Re/Ca = 10$: with an increase in bubble speed U we observe a reduction in the length

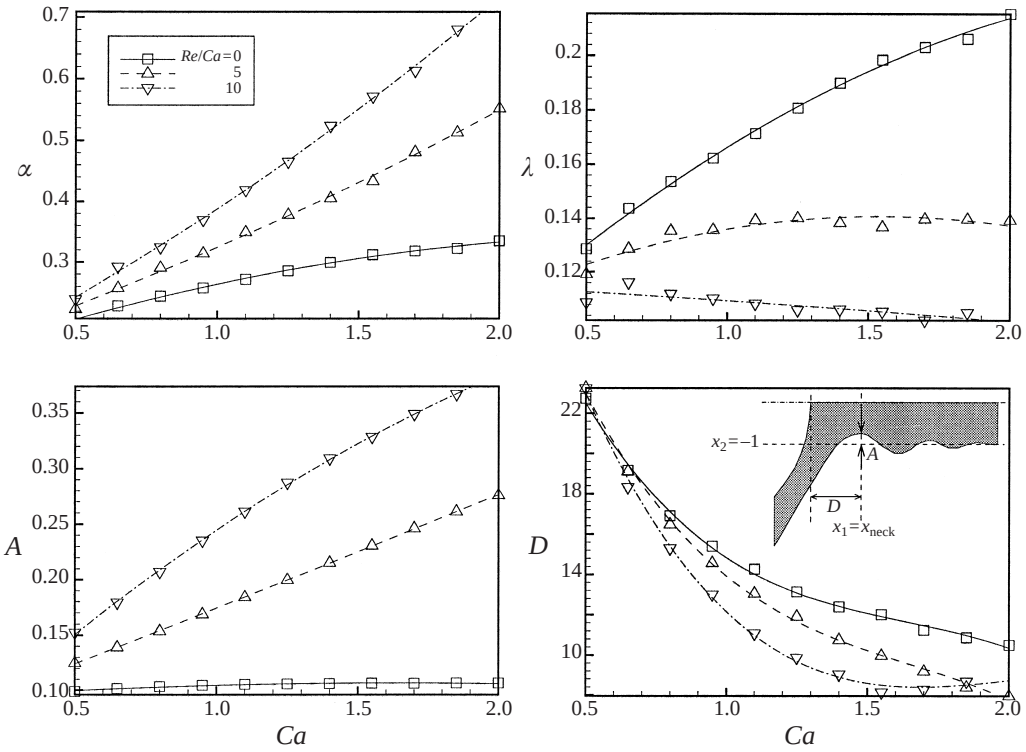

FIGURE 8. The four parameters characterizing the wall displacement field ahead of the bubble tip: A, α and λ are the amplitude, wavenumber and decay rate of the wave pattern. D is the distance between the 'neck' and the bubble tip. $\eta = 100$, $\Gamma = 0.5$.

of the transition region ahead of the bubble tip, a convenient measure of which is given by the distance D between the bubble tip and the position of the 'neck', as illustrated in the sketch in figure 8. Furthermore, figure 7 shows that the amplitude and wavenumber of the damped oscillatory wall displacement field ahead of the bubble tip increase with U. To some extent, these effects are already present at zero Reynolds number (see figure 4) but fluid inertia significantly enhances them. This is demonstrated in figure 8 which displays the four main parameters which characterize the wall displacement field ahead of the bubble tip: A, α and λ are the amplitude, wavenumber and decay rate of the wall displacement field which were obtained by approximately fitting the wall shape in this region to the function

$$x_2^{(wall)} = -1 + A\,\mathrm{e}^{-\lambda(x_1 - x_{neck})}\cos\left(\alpha(x_1 - x_{neck})\right). \tag{3.6}$$

Figure 8 shows that the wavenumber α increases with the bubble speed – more rapidly so for larger values of Re/Ca. For zero Reynolds number, an increase in bubble speed leads to an increase in the decay rate λ. This effect is reduced and finally reversed as Re/Ca increases. Finite Reynolds numbers also lead to a significant increase in the wave amplitude A and hence to an increased narrowing of the channel in the 'neck' region. It is interesting to note that similar effects have been reported in Christodoulou & Scriven's (1989) study of finite Reynolds number effects in free-surface coating flows. The length D of the transition region initially decreases with an increase in flow speed (more rapidly at larger Re/Ca) but for sufficiently large Re/Ca it increases again at larger flow speeds.

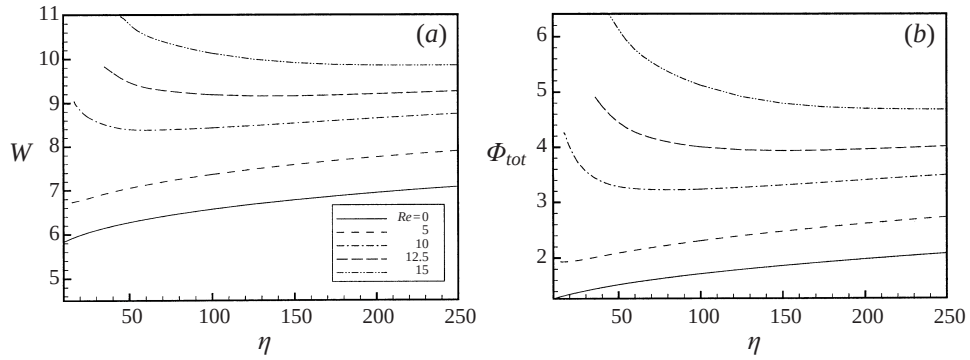

FIGURE 10. The channel width W and the total dissipation Φ_{tot} versus the wall tension parameter η for various values of Re and for $Ca = 2.0$, $\Gamma = 0.5$.

The streamlines in figure 7 suggest two potential mechanisms to explain the strong effect of fluid inertia on the system's behaviour: (i) at finite Reynolds number, the large streamline curvature near the bubble tip requires larger pressures to deflect the oncoming fluid (in the moving frame of reference) around the bubble tip; (ii) the pressure drop associated with the Bernoulli effect in the 'neck' region is responsible for the further narrowing of the channel which causes increased viscous dissipation. Note that both of these mechanisms are self-sustaining and are therefore consistent with the increasingly rapid growth in W with an increase in flow speed shown in figure 6: an increase in p_b (however caused) widens the channel behind the bubble tip and thus increases the streamline curvature further; similarly, the pressure-induced narrowing of the 'neck' region further enhances the Bernoulli effect and the viscous dissipation in the neck region, potentially leading to the occurrence of 'flow limitation' which is well known in collapsible tube theory (Kamm & Pedley 1989).

To assess the relevance of the two proposed mechanisms, figure 9 (p. 38) shows a detailed picture of the flow fields near the bubble tip for $Re/Ca = 10$. The streamlines are now plotted on top of the contours of the absolute velocity and the axis ratio in all three plots is 1:1 so that the true streamline curvature is shown. At small Reynolds number, the flow through the gently varying 'neck' region exhibits all the features suggested by lubrication theory. The velocity profile is approximately parabolic and adjusts itself immediately to the local channel width. The closed vortex ahead of the bubble tip is located in a fairly stagnant flow region. As the bubble velocity increases, fluid inertia begins to manifest itself. Even though the wall shape in the 'neck' region remains fairly symmetric, the flow field develops a distinct upstream/downstream asymmetry. To the right of the 'neck', the fluid in the core resists the acceleration; to the left of the 'neck', the high-velocity fluid on the channel's centreline maintains its momentum past the 'neck' region and impinges on the stagnant flow region ahead of the bubble tip. Note that in all cases, significant fluid velocities are only encountered in the neck region and in two relatively thin layers near the walls. The most strongly curved streamlines are located in regions of small absolute velocities which suggests that, at least for the cases shown in figure 9, finite Reynolds number effects are mainly due to mechanism (ii). This is consistent with figure 7 which shows that even at relatively large Re, the pressure remains approximately constant across the width of the channel. Nevertheless, at higher Reynolds numbers, a pressure rise towards the bubble tip can be detected – see the insert in figure 7. This pressure rise is caused by the streamline curvature in this region and leads to a reduction in interface curvature

near the bubble tip. For sufficiently large Re (and/or sufficiently low wall tension; see below) this inertially caused pressure rise can become strong enough for the interface curvature near the bubble tip to become negative: The high-velocity fluid emanating from the 'neck' region impinges on the bubble tip and makes the interface 'bulge out'. This effect is responsible for the increase in D at sufficiently large Re observed in figure 8.

3.3. *Variations of the wall parameters*

Gaver *et al.* (1996) studied the system's behaviour in response to changes in the wall parameters η and Γ. We will now investigate how the system's behaviour for such parameter variations is affected by fluid inertia.

3.3.1. *Variations in the wall tension*

Figure 10(a) shows the channel width, W, far behind the bubble tip as a function of the dimensionless wall tension, η, for $Ca = 2.0$. The different curves correspond to different values of Re. The figure shows that for any given value of η, an increase in Re increases the channel width W, as observed previously.

The main effect of an increase in wall tension is a smoothing of the wall displacement field which increases the streamwise lengthscale, as shown in figure 11. This reduces the wavenumber α and the decay rate λ of the damped oscillatory wall displacement field ahead of the bubble tip. The increase in lengthscale also increases the length D of the transition region ahead of the bubble tip. Since this is the main region in which significant velocity gradients are present, Gaver *et al.* (1996) suggested that (at zero Reynolds number) an increase in D is likely to increase the overall viscous dissipation in the system which could explain the increase in bubble pressure p_b (and hence W), required to drive the bubble at a given speed, as η increases. To test Gaver *et al.*'s (1996) hypothesis, figure 10(b) shows the total non-dimensional dissipation in the vicinity of the bubble tip,

$$\Phi_{tot} = \int_{\zeta_l<\zeta<\zeta_r} \left(\frac{\partial u_i}{\partial x_j} + \frac{\partial u_j}{\partial x_i} \right)^2 \mathrm{d}V, \tag{3.7}$$

as a function of the non-dimensional wall tension. The close correlation between the bubble pressure and the total dissipation strongly supports Gaver *et al.*'s (1996) interpretation of the results.

Figure 10(a) also shows that fluid inertia can lead to an interesting change in the $W(\eta)$ characteristics: for sufficiently small wall tension and sufficiently large Re, W increases with a *reduction* in η. A detailed analysis of the corresponding flow fields, shown in figures 11(c, d), shows that this is caused by the following mechanism. As the wall tension is reduced, the transition region shortens and moves the 'neck' closer to the bubble tip. This strongly enhances the inertial effects via mechanism (ii) because it increases the streamline curvature ahead of the bubble tip and moves the most strongly curved streamlines into regions of larger absolute velocities. A strong adverse pressure gradient towards the bubble tip develops and makes the air–liquid interface 'bulge out' while the width of the transition region increases significantly. The combination of these two effects leads to a significant increase in the total dissipation Φ_{tot} which increases the bubble pressure p_b required to drive the bubble at the given speed. Further parameter studies (not shown here) were carried out to investigate the effect of Ca on this mechanism. As shown in figure 4, a decrease in Ca increases the axial lengthscale of the wall deformation. Therefore, smaller Ca values

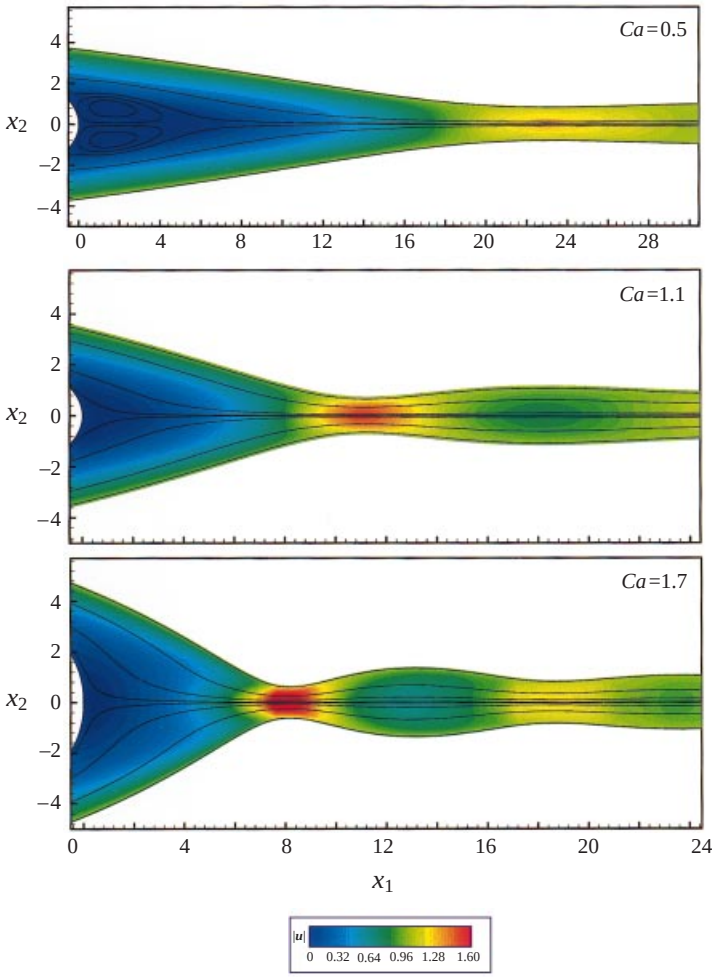

FIGURE 9

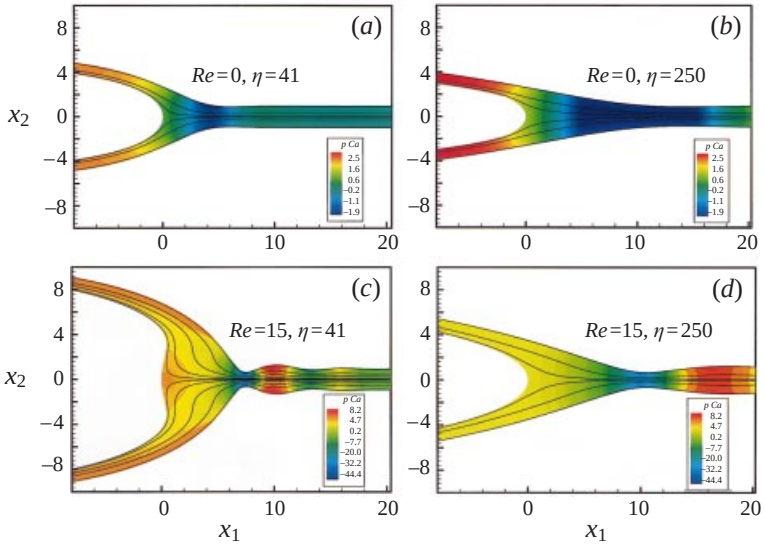

FIGURE 11

FIGURE 9. Streamlines and contours of the absolute velocity $|\boldsymbol{u}|$ for Re/Ca = 10, Γ = 0.5, η = 100. The axis ratio is 1 : 1 in all three plots so that the true streamline curvature is shown.

FIGURE 11. Streamlines and contours (on the capillary pressure scale) for Ca = 2.0, Γ = 0.5, and various combinations of Re and the wall tension η.

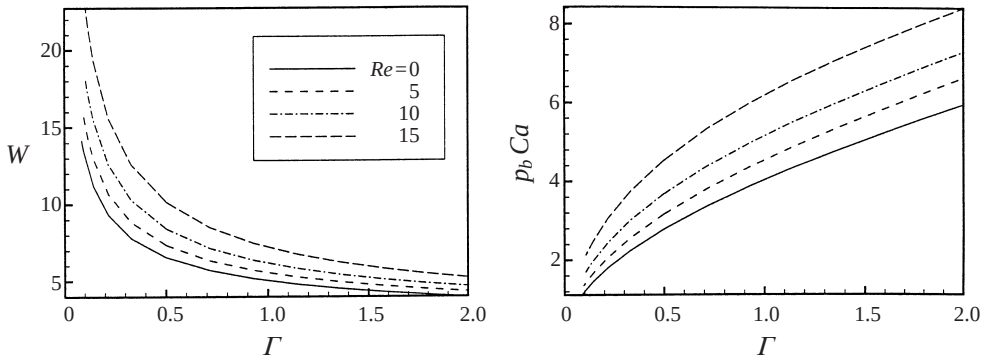

FIGURE 12. The channel width W and the bubble pressure on the capillary scale, $p_b Ca$, versus the non-dimensional spring constant Γ for various Re and for $\eta = 100$, $Ca = 2$.

require smaller values of η (or larger values of Re) to initiate the change in the $W(\eta)$ characteristics observed in figure 10(a).

It is interesting to note that the streamlines in figure 11(c) indicate that, despite the rapid expansion of the channel in the vicinity of the 'neck' region and the presence of a strong adverse pressure gradient towards the bubble tip, the moving walls prevent flow separation: The fluid which emanates from the centre of the 'neck' region appears to 'detach' from the wall and is only deflected sideways when it impinges on the bubble tip. However, the moving wall forces the fluid in the thin layer close to the walls to maintain its velocity and thus prevents the development of a recirculation bubble which would almost certainly form if the walls were stationary. It should be noted that the flow field shown in figure 11(c) is very likely to be unstable to non-symmetric perturbations which would force the flow to attach itself to one side of the channel. However, the investigation of non-symmetric solutions is beyond the scope of this paper.

3.3.2. *Variations in the spring stiffness*

Figure 12 illustrates the system's behaviour in response to changes in the non-dimensional spring stiffness Γ: a reduction in spring stiffness increases the channel width W but it also reduces the bubble pressure required to maintain the same bubble speed. Gaver *et al.* (1996) observed this behaviour at zero Reynolds number and figure 12 shows that fluid inertia only has a quantitative effect in that increasing Re increases the bubble pressure and the wall separation. Figure 13 shows that variations in the spring stiffness only have a noticeable effect in the region to the left of the 'neck': A reduction in spring stiffness reduces the rate at which the wall approaches its equilibrium position as $x_1 \to -\infty$. It also shortens the length D of the transition region ahead of the bubble tip; further parameter studies (not shown here) showed that the latter effect is more pronounced at smaller Ca. Gaver *et al.* (1996) suggest that, as in the analysis of variations of the wall tension, this reduction in D reduces the total viscous dissipation in the fluid. This explains why a reduction in spring stiffness reduces the bubble pressure p_b required to maintain the same bubble speed. In the parameter range considered in the present study, the reduction in D was never sufficient to increase the inertial effects to such an extent that they lead to an increase in p_b at small values of Γ as in the case of a reduction in η.

In contrast to the significant changes to the wall displacement field behind the bubble tip, the damped oscillatory wall displacement field ahead of the 'neck' remains virtually unaffected by changes to the spring stiffness: an increase in Γ slightly

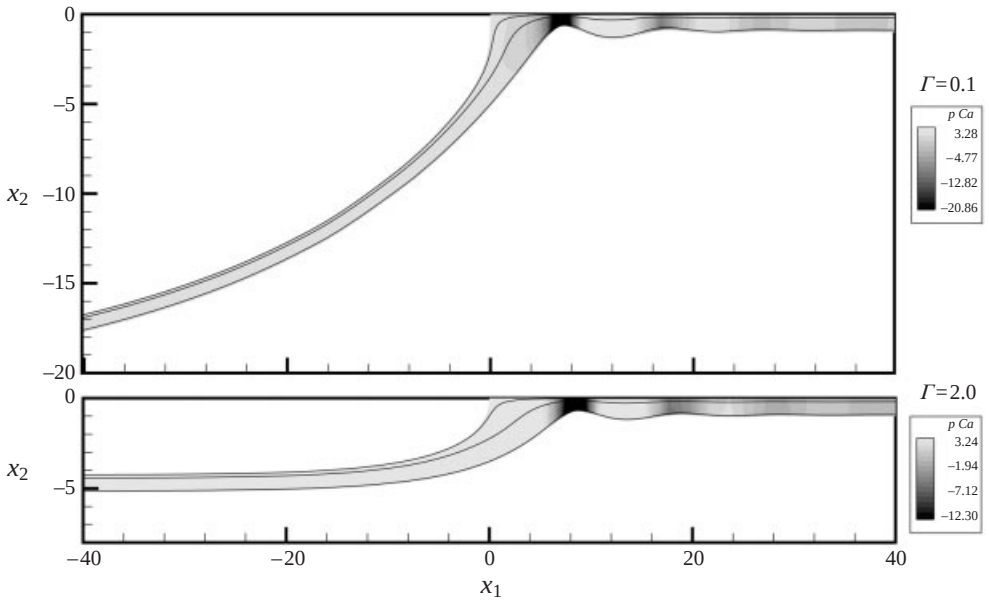

FIGURE 13. Streamlines and pressure contours (on the capillary pressure scale) for $\Gamma = 0.1$ and $\Gamma = 2.0$. $\eta = 100$, $Re = 15$, $Ca = 2.0$.

reduces its amplitude A (more rapidly at smaller Ca) but for all Reynolds numbers, its wavenumber α and decay rate λ are practically independent of Γ.

3.3.3. *Variations in γ and h_0/H_0*

Within their physically relevant ranges, variations of the non-dimensional surface tension, γ, and the non-dimensional wall thickness, h_0/H_0, only have a minor effect on the system's behaviour. The variations in response to changes in γ, shown in figure 3 (for $Re = 0$) are also representative of the behaviour at finite Reynolds number. An increase in wall thickness increases the wall's bending stiffness and slightly increases the bubble pressure p_b required to drive the bubble at a given speed. The effect is more pronounced in cases where the streamwise lengthscale of the wall deformation is relatively short (i.e. for larger values of Ca) but the effect on the $p_b(Ca)$ relation remains fairly small. For instance, for $Ca = 2.0$, $\Gamma = 0.5$, $\eta = 100$ an increase from the standard value of $h_0/H_0 = 5 \times 10^{-4}$ to $h_0/H_0 = 1/10$ only increases p_b by 3.5% for $Re = 0$ and by 3.0% for $Re = 15$.

4. Discussion

To assess the significance of the above results in the context of the airway reopening problem, we will now provide estimates for the relevant parameter values in the typical benchtop experiments (Gaver *et al.* 1990 and Perun & Gaver 1995) and in the lung airways. The most important parameter in the present study was shown to be the ratio of the Reynolds and capillary numbers, which depends strongly on the viscosity of the fluid; see (3.5). Table 1 shows that for the experiments with gear oil, Re/Ca is indeed small enough to justify the neglect of fluid inertia. However, the present results suggest that inertial effects might have played a role in the experiments with some of the other fluids, particularly with polyethylene glycol. It is interesting to note that Perun & Gaver's (1995) experimental reopening pressures, $p_b(Ca)$, are generally above

Medium [reference]	ρ [kg m^{-3}]	γ^* [dyn cm^{-1}]	H_0 [mm]	μ [dyn s cm^{-2}]	Re/Ca
85W gear oil [GS&S]	930	25.0	0.83	9.9	0.02
85W gear oil [P&G]	930	30.9	0.83	7.4	0.04
10W30 motor oil [GS&S]	890	24.7	0.83	1.5	0.81
10W30 motor oil [P&G]	890	28.4	0.83	0.72	4.04
Polyethylene glycol [GS&S]	1140	42.4	0.83	1.1	3.31
Polyethylene glycol [P&G]	1140	45.3	0.83	0.83	6.24
Lung fluid in collapsed bronchioli [H&G]	1000	20.0	0.025	0.01	500

TABLE 1. Re/Ca for typical laboratory experiments with viscous fluids and for lung fluid in a collapsed airway. References: [P&G] = Perun & Gaver (1995), [GS&S] = Gaver *et al.* (1990), [H&G] = Halpern & Grotberg (1992).

the values obtained from Gaver *et al.*'s (1996) zero Reynolds number computations. A direct comparison, provided in Jensen *et al.* (2000), shows that the difference between the computational data (at zero Reynolds number) and the experimental data is of the same order of magnitude as the pressure difference due to fluid inertia shown in figure 6.

Airway closure in the lung tends to occur in the peripheral parts of the bronchial tree in which the lung fluid has water-like properties (Grotberg 1994). We consider airway reopening in the terminal bronchioli and assume that airway closure has collapsed them to a width H_0 which is equal to 1/10 of their undeformed radius a. Using the data provided by Halpern & Grotberg (1992), $a = 2.5 \times 10^{-2}$ cm, we obtain a surprisingly large value of $Re/Ca = 500$. Considering possible variations of the parameter values, we see that a surfactant-induced reduction in surface tension (by a factor of 2–3; Halpern & Grotberg 1993) would lead to a proportional reduction in Re/Ca; moving into the larger airways would increase Re/Ca in proportion to the airway radius. The value of Re/Ca in the lungs certainly appears to be large enough for inertial effects to be potentially significant in airway reopening.

Lung airways tend to have a greater non-dimensional wall thickness h_0/H_0 than the channels considered in this study or the very thin-walled tubes used in the experiments. However, the parameter variations discussed in § 3.3.3 suggest that variations in the wall thickness only have a very moderate effect on the results and will not significantly affect the system's qualitative behaviour.

A concern regarding the applicability of the present results to airway reopening in the lungs arises from the difference in the spatial dimension between the model problem and the three-dimensional lung airways. In a two-dimensional model there is no fundamental difference between 'inflated' and 'collapsed' states since an overall increase in the fluid pressure results in a uniform expansion of the channel – this can be accommodated by an appropriate rescaling of the variables, as indicated in the introduction. Hence, in a two-dimensional model, the transmural pressure in the liquid-filled, collapsed part of the channel far ahead of the bubble tip, $p_{tm(\infty)} = (p - p_{ext})\,|_{x_1 \to \infty}$, is irrelevant – we arbitrarily set it to zero. This is in contrast to the three-dimensional system in which the airway radius R_0 provides a natural transverse lengthscale: in three dimensions, a change in transmural pressure is not equivalent to a simple change in the transverse lengthscale. In the experimental or physiological realization of airway reopening, p_{ext} and p_b are imposed while the bubble velocity and $p_{tm(\infty)}$ are allowed to adjust themselves. In this situation $p_{tm(\infty)}$ is one of the most important

parameters: if $p_{tm(\infty)} = 0$ (the case chosen here) then far ahead of the bubble tip the tube is undeformed. Hence, the propagating air finger would not reopen a non-axisymmetrically collapsed tube but merely inflate an axisymmetric tube even further. Clearly, this is not representative of the situation in airway reopening which requires $p_{tm(\infty)}$ to be sufficiently negative so that the fluid-filled part of the tube is buckled non-axisymmetrically. The extension of the computational model to three dimensions, which will allow this problem to be properly investigated, is currently in progress.

From an analytical point of view, it will be interesting to further analyse the mechanism governing the pronounced changes to the wave pattern in the wall displacement field ahead of the bubble tip as the Reynolds number increases. The fact that the computational results show that the pressure distribution ahead of the bubble tip is approximately uniform across the channel suggests that a long-wavelength analysis, similar to that used by Christodoulou & Scriven (1989) might be appropriate.

An anonymous referee pointed out that the wave pattern ahead of the bubble tip has some similarity to the waves that appear ahead of an elastic jump in the supercritical region of flow through a collapsible tube. McClurken *et al.*'s (1981) analysis of the latter problem showed that these waves can be regarded as travelling waves which emanate from the expansion region and become trapped because their local phase speed is equal (and opposite) to the fluid velocity. McClurken *et al.*'s (1981) analysis predicts a decrease in the wavelength with an increase in the flow velocity. Figure 8 shows that this is qualitatively consistent with the present results.

The author would like to thank Don Gaver, Oliver Jensen and David Halpern for many helpful and enjoyable discussions and for providing him with a preprint of Jensen *et al.* (2000) as well as the data for the comparison of the two wall models in figure 3(*a*). Further thanks are due to Francoise Tisseur for drawing the author's attention to Demmel *et al.*'s (1999) SuperLU solver and for her help with its installation. Financial support from the EPSRC is gratefully acknowledged.

Appendix. Lubrication theory and the end conditions at $x_1 \to \pm\infty$

Far ahead of the bubble tip, the walls become nearly parallel so that the fluid flow can be described by lubrication theory. Furthermore, the wall strain becomes so small that $\mathrm{d}\zeta \approx \mathrm{d}x_1$. Hence, the non-dimensional pressure gradient (in the wall non-dimensionalization) in this region is given by

$$\frac{\mathrm{d}p}{\mathrm{d}\zeta} = 3\,Ca\,\gamma\frac{v^2}{(1-v^2)^3}. \tag{A 1}$$

Equation (A 1) was used to determine the fluid pressure in the region $\zeta > \zeta_r$ ahead of the Navier–Stokes domain. Correspondingly, the wall shear stress in this region was obtained from

$$\tau_w = -3\,Ca\,\gamma\frac{v^2}{(1-v^2)^2}. \tag{A 2}$$

The finite element discretization of the wall itself is truncated at a finite distance ahead of the bubble tip, at $\zeta = \zeta_R$. For small Ca, the wall remains inflated over a large distance ahead of the bubble tip. In order to truncate the computational domain at reasonable distances, the effect of the domain in the region $\zeta > \zeta_R$ was incorporated by representing the wall displacement field at large distances by the appropriate decaying eigenfunctions. For this purpose we chose ζ_R to be large enough to ensure

that the derivatives of the wall displacements at $\zeta = \zeta_R$ have become small. Then the linearized forms of the variational expressions for the vertical wall displacement,

$$\phi_2^{(0)} = p + Kv^2, \quad \phi_2^{(1)} = \gamma\,\eta\; v_{,\zeta}^2 \quad \text{and} \quad \phi_2^{(2)} = \frac{1}{12}\left(\frac{h_0}{H_0}\right)^3 v_{,\zeta\zeta}^2 \tag{A 3}$$

are valid. We derive the corresponding Euler Lagrange equation, differentiate it with respect to ζ and substitute the linearized form of the lubrication theory pressure gradient from (A 1). This yields a fifth-order ODE with constant coefficients for v^2. Only three roots, Λ, of the characteristic polynomial

$$\frac{1}{12}\left(\frac{h_0}{H_0}\right)^3 \Lambda^5 - \gamma\eta\Lambda^3 + \Gamma\gamma\Lambda + 3\gamma\, Ca = 0 \tag{A 4}$$

have negative real part. The decaying eigenfunction for the vertical wall displacement can be shown to have the form

$$v^2 = C_1\,\mathrm{e}^{-\theta\zeta} + \mathrm{e}^{-\lambda\zeta}\left(C_2\cos(\alpha\zeta) + C_3\sin(\alpha\zeta)\right), \tag{A 5}$$

where $\theta \gg \lambda > 0$. Compared to Gaver *et al.*'s (1996) analysis, we have one additional rapidly decaying eigensolution (associated with θ) which arises from the bending stiffness in the system.

To incorporate these eigensolutions into the finite element solution of the wall equations, we express the coefficients C_1, C_2 and C_3 in (A 5) in terms of the vertical displacement and its first and second derivatives at the right-hand end of the computational domain (at $\zeta = \zeta_R$). The finite element representation of the displacement field (2.3) allows us to express C_1, C_2 and C_3 in terms of the discrete displacements V^{ijk}. We split the domain of integration in the variational equation (2.2) into three parts such that

$$\int_{-\infty}^{\infty} \delta\phi\,\mathrm{d}\zeta = \int_{-\infty}^{\zeta_L} \delta\phi\,\mathrm{d}\zeta + \int_{\zeta_L}^{\zeta_R} \delta\phi\,\mathrm{d}\zeta + \int_{\zeta_R}^{\infty} \delta\phi\,\mathrm{d}\zeta = 0. \tag{A 6}$$

The second integral has already been discretized. The variational terms in the third integral can be approximated by the linearized expressions (A 3) and the eigensolution (A 5) determines their spatial variation. Hence the integral can be evaluated analytically (using MAPLE) and the variations become variations with respect to the discrete displacements V^{ijk}. Collecting the terms which are multiplied by the same δV^{ijk} provides the corresponding end terms Φ_{ijk} in (2.5).

The non-zero wall shear stress in the region $\zeta > \zeta_R$ implies that the wall tension at $\zeta = \zeta_R$ is not equal to the asymptotic value σ_0: a global balance of forces shows that

$$\sigma\,|_{\zeta=\zeta_R} = \sigma_0 + \left(\frac{H_0}{h_0}p(1-v^2)\right)\Bigg|_{\zeta=\zeta_R}. \tag{A 7}$$

The work done by a virtual horizontal displacement δv^1 at the right-hand end of the domain is given by $(\sigma\ \delta v^1)|_{\zeta=\zeta_R}$. Again, we use the finite element representation (2.3) to express δv^1 in terms of the variations of the discrete displacements, δV^{ijk}, which allows us to identify the remaining end-terms Φ_{ijk} in (2.5).

Far behind the bubble tip, the Navier–Stokes domain is truncated at $\zeta = \zeta_l$ and the fluid traction on the wall in the region $\zeta_L < \zeta < \zeta_l$ was determined from a thin-film lubrication theory approximation similar to Gaver *et al.* (1996). The computational studies revealed that as $\zeta \to -\infty$, the film thickness approaches its final value much more rapidly than the vertical wall displacement v^2. This motivated the following

approximation which was found to produce perfectly acceptable results: the fluid traction on the wall in the region $\zeta < \zeta_l$ was assumed to be constant and equal to the value at the left-hand end of the Navier–Stokes domain at $\zeta = \zeta_l$; furthermore, a value of $\zeta_L = -300$ was found to be sufficient to resolve the approach of the vertical wall displacement v^2 to its final value $v^2 \to W - 1$, which allowed us to completely neglect the contribution from the first integral in (A 6).

REFERENCES

Bretherton, F. P. 1961 The motion of lung bubbles in tubes. *J. Fluid Mech.* **10**, 166–188.

Bogner, F. K., Fox, R. L. & Schmit, L. A. 1967 A cylindrical shell discrete element. *AIAA J.* **5**, 745–750.

Christodoulou, K. N. & Scriven, L. E. 1989 The fluid mechanics of slide coating. *J. Fluid Mech.* **208**, 321–354.

Demmel, J. W., Eisenstat, S. C., Gilbert, J. R., Li, X. S. & Liu, J. W. H. 1999 A supernodal approach to sparse partial pivoting. *SIAM J. Matrix Anal. Applics.* **20**, 720–755.

Gaver, D. P. III, Halpern, D., Jensen, O. E. & Grotberg, J. 1996 The steady motion of a semi-infinite bubble through a flexible walled channel. *J. Fluid Mech.* **319**, 25–56.

Gaver, D. P., Samsel, R. W. & Solway, J. 1990 Effects of surface tension and viscosity on airway reopening. *J. Appl. Physiol.* **69**, 74–85.

Giavedoni, M. D. & Saita, F. A. 1997 The axisymmetric and plane cases of a gas phase steadily displacing a Newtonian liquid – A simultaneous solution of the governing equations. *Phys. Fluids* **9**, 2420–2428.

Grotberg, J. B. 1994 Pulmonary flow and transport phenomena. *Ann. Rev. Fluid Mech.* **26**, 529–571.

Heil, M. & Pedley, T. J. 1996 Large post-buckling deformations of cylindrical shells conveying viscous flow. *J. Fluids Struct.* **10**, 565–599.

Halpern, D. & Grotberg, J. B. 1992 Fluid-elastic instabilities of liquid-lined flexible tubes. *J. Fluid Mech.* **244**, 615–632.

Halpern, D. & Grotberg, J. B. 1993 Surfactant effects on fluid-elastic instabilities of liquid-lined flexible tubes: a model of airway closure. *ASME J. Biomech. Engng* **115**, 271–277.

Hughes, J. M. B., Rosenzweig, D. Y. & Kivitz, P. B. 1970 Site of airway closure in excised dog lungs: histologic demonstration. *J. Appl. Physiol.* **29**, 340–344.

Jensen, O. E., Horsburgh, M. K. & Gaver, D. P. 2000 The steady propagation of a bubble in a flexible-walled channel: asymptotic and computational models. *Phys. Fluids* (submitted).

Kamm, R. D. & Pedley, T. J. 1989 Flow in collapsible tubes: a brief review. *J. Biomech. Engng* **111**, 177–179.

Kistler, S. F. & Scriven, L. E. 1983 Coating flows. In *Computational Analysis of Polymer Processing* (ed. J. R. A. Pearson & S. M. Richardson). Applied Science Publishers, London.

Macklem, P. T., Proctor, D. F. & Hogg, J. C. 1970 The stability of the peripheral airways. *Respir. Physiol.* **8**, 191–203.

McClurken, M. E., Kececioglu, I., Kamm, R. D. & Shapiro, A. H. 1981 Steady, supercritical flow in collapsible tubes. Part 2. Theoretical studies. *J. Fluid Mech.* **109**, 391–415.

Perun, M. L. & Gaver, D. P. 1995 Interaction between airway lining fluid forces and parenchymal tethering during pulmonary airway reopening. *J. Appl. Physiol.* **79**, 1717–1728.

Pride, N. B. & Macklem, P. T. 1986 Lung mechanics in disease. In: *Handbook of Physiology. Section 3: The Respiratory System*, Vol. III, Part 2, pp. 659–692. American Physiological Society.

Ruschak, K. J. 1980 A method for incorporating free boundaries with surface tension in finite element fluid-flow simulators. *Intl J. Numer. Meth. Engng* **15**, 639–648.

Sani, R. L., Gresho, P. M., Lee, R. L. & Griffith, D. F. 1981 The cause and cure (?) of the spurious pressures generated by certain FEM solutions of the incompressible Navier–Stokes equations: Part I. *Intl J. Numer. Meth. Fluids* **1**, 17–43.

Wempner, G. 1973 *Mechanics of Solids*. McGraw-Hill.

Yap, D. Y. K., Liebkemann, W. D., Solway, J. & Gaver, D. P. 1994 Influences of parenchymal tethering on the reopening of closed pulmonary airways. *J. Appl. Physiol.* **76**, 2095–2105.